Phase-Selective Doping of Oriented Regioregular Poly(3-hexylthiophene-2,5-diyl) Controls Stability of Thermoelectric Properties

Shubhradip Guchait, Aditya Dash, Antoine Lemaire, Laurent Herrmann, Martijn Kemerink, Martin Brinkmann

Phase-selective doping of oriented regioregular poly(3-hexylthiophene-2,5-diyl) controls stability of thermoelectric properties

Shubhradip Guchait[1+], Aditya Dash[2+], Antoine Lemaire[1], Laurent Herrmann[1], Martijn Kemerink[2], Martin Brinkmann[1]*

(1) Institute Charles Sadron, UPR022 CNRS - University of Strasbourg, 23 rue du loess, 67034 Strasbourg, France

(2) Institute for Molecular Systems Engineering and Advanced Materials, Heidelberg University, Im Neuenheimer Feld 225, 69120 Heidelberg, Germany

* corresponding author e-mail: martin.brinkmann@ics-cnrs.unistra.fr

+ The two authors contributed equally to this work.

Abstract

This study focuses on the impact of dopant location in the semi-crystalline structure of regioregular poly(3-hexylthiophene-2,5-diyl) on the long-term stability of thermoelectric properties probed in rub-aligned thin films. Phase-selective doping is possible by suitable choice of dopants. Anion exchange doping results in TFSI dopants located in both crystalline and amorphous domains whereas magic blue dopants are located in the amorphous phase only. First, we demonstrate that the combination of rub-alignment, increasing concentration doping and anion exchange doping is effective to produce doped P3HT films with enhanced thermoelectric properties and stability. Transmission electron microscopy, polarized optical absorption spectroscopy and transport measurements help identify different regimes of doping: crystalline domains are doped first by exchange of F_4TCNQ^- with $TFSI^-$, followed by a progressive doping of amorphous regions of P3HT. The best thermoelectric performances of TFSI-exchanged P3HT lead to power factors in the 160-170 $\mu W/mK^2$ range. Despite similar TE performances after preparation, MB-doped and TFSI-exchanged P3HT films behave very differently on ageing. Numerically exact kinetic Monte Carlo simulations clarify the origin of this difference. The retention of charges in any phase is crucial for the stability in conductivity, but the conductivity at long ageing times, σ_∞ is quantitatively determined by the specific phase capable of retaining the charges.

I. Introduction.

Doping of polymer semiconductors (PSCs) has become a central topic in organic electronics as it helps tune the carrier density and hence charge transport properties in thin films and devices.[1] More specifically, doping PSCs such as P3HT or PBTTT is the method of choice to fabricate thermoelectric (TE) polymer films.[2-5] Different doping methods have been investigated so far, e.g. mixing the polymer and dopant in a common solvent or sequential doping of the PSC from solution or from the vapor phase.[3] p-type doping involves either strong acceptor molecules such as F_4TCNQ or strong Lewis acids such as $FeCl_3$.[6] In the case of the semi-crystalline polymer P3HT, phase-selective doping is possible. The molecular dopant can be introduced in either the amorphous, the crystalline or both phases. Dopants such as F_4TCNQ and F_6TCNNQ are preferentially intercalated into the side chain layers between π-stacks of P3HT[7,8] leading to integer charge transfer. In this case, the structure of the pristine P3HT is strongly modified and new so-called co-crystals can form depending on the stabilization of the dopant ion inside the polymer matrix.[7,10,11] Under specific preparation conditions, charge transfer complexes may be formed when the dopant and conjugated polymer π-stack.[9] The possibility to dope amorphous and/or crystalline domains further depends on the electron affinity of the dopant. F_4TCNQ and F_6TCNNQ cannot transfer a charge to the disordered P3HT chains in the amorphous phase whereas stronger dopants such as $FeCl_3$ or $NOPF_6$ can. Notably, the dopant tris(4-bromophenyl)ammoniumyl hexachloroantimonate (magic blue) can dope both crystalline and amorphous zones while being located essentially in the amorphous zones of P3HT.[12,13] Such a nanoscale segregation in the doping of P3HT results in a spatial separation of the counterions of $SbCl_6^-$ (in the amorphous phase) from the mobile charge carriers present in the crystalline phase. This structural organization helps reach high charge conductivities of up to 3000 S/cm at relatively low dopant concentrations in oriented P3HT films and thermoelectric power factors

of up to 170 μW/mK^2.[13] A mechanism of so-called spontaneous modulation doping was introduced by Dash et al. to explain the beneficial effect of phase-selective doping of P3HT with MB.[14]

Effective doping of PSCs requires dopants with strong electron affinity. The palette of existing redox molecules is limited however and strong dopants such as $FeCl_3$ lead to unstable systems with a loss of transport properties within a few hours, even under inert atmosphere.[15] Chabinyc and coworkers suggested that the stability of doped PSCs relates at least in part to the resistance of counter-ions to degradation.[16] Recently, Watanabe et al. proposed an elegant method to introduce stable and very effective dopants into PSCs using the method of anion exchange.[17,18] When a PSC film is exposed to a solution of the redox dopant F_4TCNQ and the ionic salt LiTFSI, the anion F_4TCNQ^- is exchanged with $TFSI^-$. The optimal ratio of redox dopant and ionic salt helps induce an almost complete anion exchange in the PSC, whereby much higher charge carrier densities of up to $1x10^{21}$ cm^{-3} can be attained after anion exchange.[19] In addition, TFSI-doped polymers are shown to be more stable than F_4TCNQ or $FeCl_3$-doped systems.[18] Other dopants such as $FeCl_3$ were also used to trigger ion exchange doping with efficiencies beyond 99% when associated with TFSI.[19,20] In parallel, the essential role of the crystallinity of the PSC prior and after doping was highlighted by numerous groups.[5,21-23] Other strategies including side chain engineering and double doping were also shown to help improve transport properties in doped PSCs used for thermoelectric applications.[24-26]

Orientation of polymers e.g. using the method of high temperature rubbing is a very effective method to control in-plane chain orientation as well as crystallinity of P3HT thin films that impacts further thermoelectric properties in thin films.[27,28] The orientation of such films is quantified by the 1D order parameter (OP) retrieved from the dichroic ratio OP=(DR-1)/(DR+2) and values as high as 0.85 could be obtained; OP=1 for a perfectly aligned film. Doping of such aligned films results in conducting polymer films with improved conductivities in the chain

direction.[5,7,13,15] In particular, introducing the dopants progressively into the crystal lattice of P3HT by so-called increasing concentration doping helped improve thermoelectric power factors in oriented thin films of P3HT and PBTTT. [5,7]

In this study, we combine anion exchange doping, incremental concentration doping and rub-alignment to produce oriented and conducting P3HT films doped with TFSI and a very high doping level in effect, comparable to that obtained with strong dopants such as magic blue. We demonstrate the impact of increasing dopant concentration on the exchange efficiency $F_4TCNQ^- \rightarrow TFSI^-$ and relate the structural changes to spectroscopic and transport properties of the doped films. We probe the stability of doped P3HT films over 40-50 days under inert atmosphere (glovebox) using charge conductivity and polarized UV-vis-NIR spectroscopy. The main finding is that stability and leveling of TE performances in doped P3HT films depends on the location of dopant molecules in the semi-crystalline structure of P3HT. When dopants are hosted in the amorphous phase of P3HT, the conductivity is almost completely lost after 50 days whereas the films doped by incremental anion exchange doping (ICAED) i.e. $TFSI^-$ anions are present in both amorphous and crystal phases of P3HT retain a stabilized value of 40% of the initial conductivity and thermoelectric power factor. Overall, this study underlines the essential role of dopant location in the microstructure of a PSC on the ageing and stability of doped PSCs.

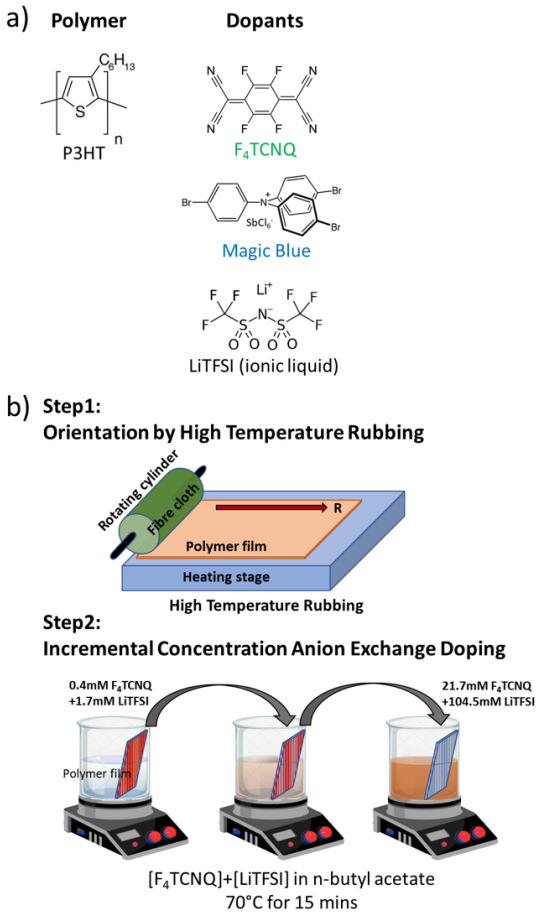

Figure 1*. a) Chemical structures of polymer and dopants used in this study. b) Method to prepare oriented and doped P3HT films in two steps: alignment by high-T rubbing and doping using the incremental concentration anion exchange method (see text).*

II. Results.

1. Anion exchange doping of oriented P3HT films.

With the perspective to reach high doping levels and enhanced stability in doped and aligned P3HT films, we developed a doping method that combines the benefits of anion exchange and incremental concentration doping to preserve best the order of the pristine PSC by smooth dopant introduction in the crystals (see **Figure 1**). The doping conditions of Incremental Concentration Anion Exchange Doping (ICAED) were first optimized to obtain reproducibly well-doped P3HT films. Optimal doping is observed at 70°C in mixtures of F_4TCNQ/LiTFSI

(1/5 ratio) in *n*-butyl acetate. The doping level is increased progressively, by sequential dipping of the rub-aligned P3HT films in solutions of the F_4TCNQ/LiTFSI mixture of increasing concentration while keeping the dipping time constant.

Polarized UV-vis-NIR spectroscopy. The effect of ICAED on the P3HT films was first followed by polarized UV-vis-NIR spectroscopy. The choice of the light polarization (POL) with respect to the chain direction (rubbing direction R) helps probing the crystalline domains for POL//R and the amorphous domains for POL⊥R. In **Figure 2**, the evolution of the spectrum for POL//R and POL⊥R with increasing doping concentration (ratio F_4TCNQ/LiTFSI=5) reveals several interesting points. Three stages of doping are identified. For [F_4TCNQ]≤3.6 mM and for POL⊥R, which predominantly probes the amorphous regions as the transition dipole moment of P3HT is parallel to the backbone direction, the spectrum is dominated by the vibronic structure of the F_4TCNQ^- anion with small contributions from polaronic bands and an almost unchanged absorption of neutral amorphous P3HT. For POL//R, which probes both the crystalline and amorphous regions, polaronic bands P1 and P2 with almost identical absorbances at their maximum coexist with a substantial absorption of neutral P3HT, indicating incomplete oxidation (see Figure 2). These observations indicate that at low doping levels the amorphous phase of P3HT is marginally doped and that the dominant species in the films are F_4TCNQ^- ions located in P3HT crystals. Increasing the concentration of the F_4TCNQ/LiTFSI solution beyond 10 mM induces major changes: i) a strong bleaching of the neutral absorption bands (N_c and N_a) of both crystalline and amorphous P3HT, ii) a strong increase of P1 and P2 absorption for POL⊥R indicating doping of the amorphous phase of P3HT and iii) the quasi disappearance of the F_4TCNQ^- absorption features. Analyzing the spectra carefully shows that ~13% of the original amount of F_4TCNQ^- is retained in the films after exchange doping at 21.7 mM. Anion exchange is incomplete in P3HT (87%) as compared to PBTTT (98%).[17] Moreover,

as indicated by the decrease in the absorbance of F_4TCNQ^-, our study shows that anion exchange starts first in the crystalline regions for 1.8mM≤ [F_4TCNQ] ≤3.6 mM. Concentrations ≥ 10.8 mM are necessary to start doping the amorphous zones of P3HT.

To understand the driving force determining the $TFSI^-$ distribution in $TFSI^-$- exchanged *vs.* F_4TCNQ-doped films, we propose a similar mechanism as in our previous work.[14] We argued that the counterion distribution is the result of a competition between the density of available sites (voids) and counterion stabilization energy in the host polymer structure. Although the void density is largest in the amorphous phase, doping P3HT with F_4TCNQ initially occurs in the crystalline phase where ICT occurs (the non-planar chain conformation of P3HT in amorphous domains prevents ICT with F_4TCNQ). Then, the high void density in the amorphous phase will act as the dominant factor in determining the counterion distribution, driving the the $TFSI^-$ ions from the P3HT crystals where the exchange with F_4TCNQ^- takes place into the amorphous phase. This last mechanism involves $TFSI^-$ counterion diffusion from crystals into the voids of the amorphous phase.

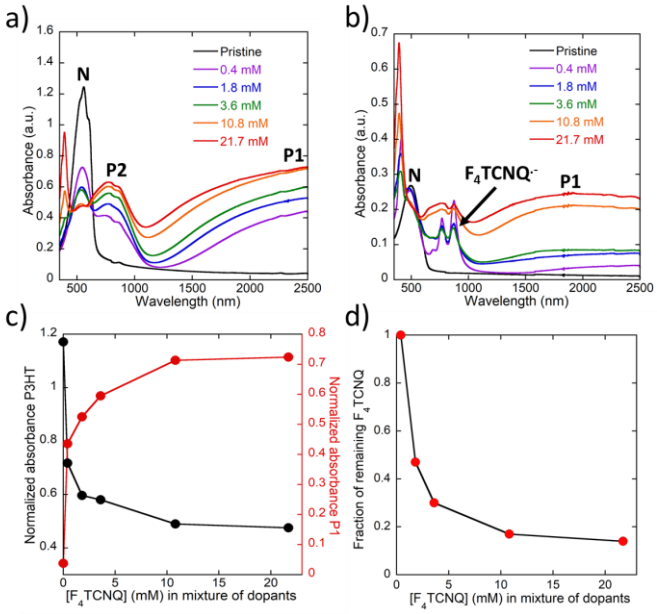

Figure 2*. a) Evolution of the polarized UV-vis-NIR spectrum of oriented P3HT films as a function of the concentration of F_4TCNQ in the blend solution of F_4TCNQ/LiTFSI blends (1:5*

ratio, 70°C) in n-BA for light polarized parallel (a) and perpendicular (b) to the rubbing direction R. c) Evolution of the P1 polaron band absorbance at 2500nm (POL//R) and of the neutral absorption (N) at 550 nm of P3HT for POL//R versus F_4TCNQ concentration in F_4TCNQ/LiTFSI blends (1:5 ratio, 70°C) in n-BA. d) Fraction of F_4TCNQ^- anion extracted from the absorption spectrum.

FTIR spectroscopy. Further insight into the doping mechanism and in particular the substitution of $F_4TCNQ^{\cdot -}$ by $TFSI^-$ can be obtained using FTIR spectroscopy. The C≡N stretching mode around 2191 cm^{-1} (see **Figure S1**) is characteristic for Integer Charge Transfer (ICT) and can be followed upon doping. As seen in **Figure S1**, the intensity of this band is strongest at the low concentration of 0.4 mM and decreases until it almost disappears at 3.6 mM. It is replaced by two types of bands: i) two bands at 2220 cm^{-1} and 2227 cm^{-1} attributed to neutral F_4TCNQ in excess on the film surface when doping at a high concentration above 10.8 mM and ii) an intense band peaked around 2200 cm^{-1} whose position is close to the charge transfer complex (CTC) band reported for P3HT/F_4TCNQ.[29,30] More generally, the position of the C≡N stretching is related to the charge density on the F_4TCNQ molecules and the shift $\Delta\nu$ between the neutral and the charged F_4TCNQ is a function of the charge δ transferred to the molecule following the relation.[31] Using this equation, the band seen at 2200 cm^{-1} should correspond to non-integer charge transfer of approximately 0.8 e^-. As stressed in earlier work, this band is associated with a localized polaronic species of P3HT.[31] It suggests that upon progressive substitution of F_4TCNQ^- by $TFSI^-$, some trapped F_4TCNQ^- molecules remain in the films, in agreement with the UV-vis-NIR results showing that only a part of F_4TCNQ^- is replaced by $TFSI^-$ upon anion exchange. The FTIR analysis suggests that the anion exchange mechanism induces a change ICT→CTC of the F_4TCNQ^- trapped in the P3HT films. Such a change would

be consistent with the indication of a diffusion of F_4TCNQ^- out of the crystalline zones into the amorphous zones at high doping concentration.

Structural changes probed by TEM. Let us observe the changes in P3HT structure induced by ICAED. **Figure 3** depicts the evolution of the ED patterns for oriented P3HT films doped at different concentrations as well as the evolution of the reticular distances d_{100} (lamellar periodicity) and d_{020} (π-stacking) (see **Figure 3**). At doping concentrations below 1.8 mM, the changes in lattice parameters mimic the ones reported for P3HT doped with F_4TCNQ: the lattice expands along the chain direction with d_{100} increasing from 16.5 Å to 18.4 Å and the π-stacking periodicity is strongly reduced from 3.80 Å to 3.57 Å. For higher concentrations, the situation changes along the π-stacking that tends to increase and recover partially the original value (d_{020}=3.70 Å at 10.8mM/l).

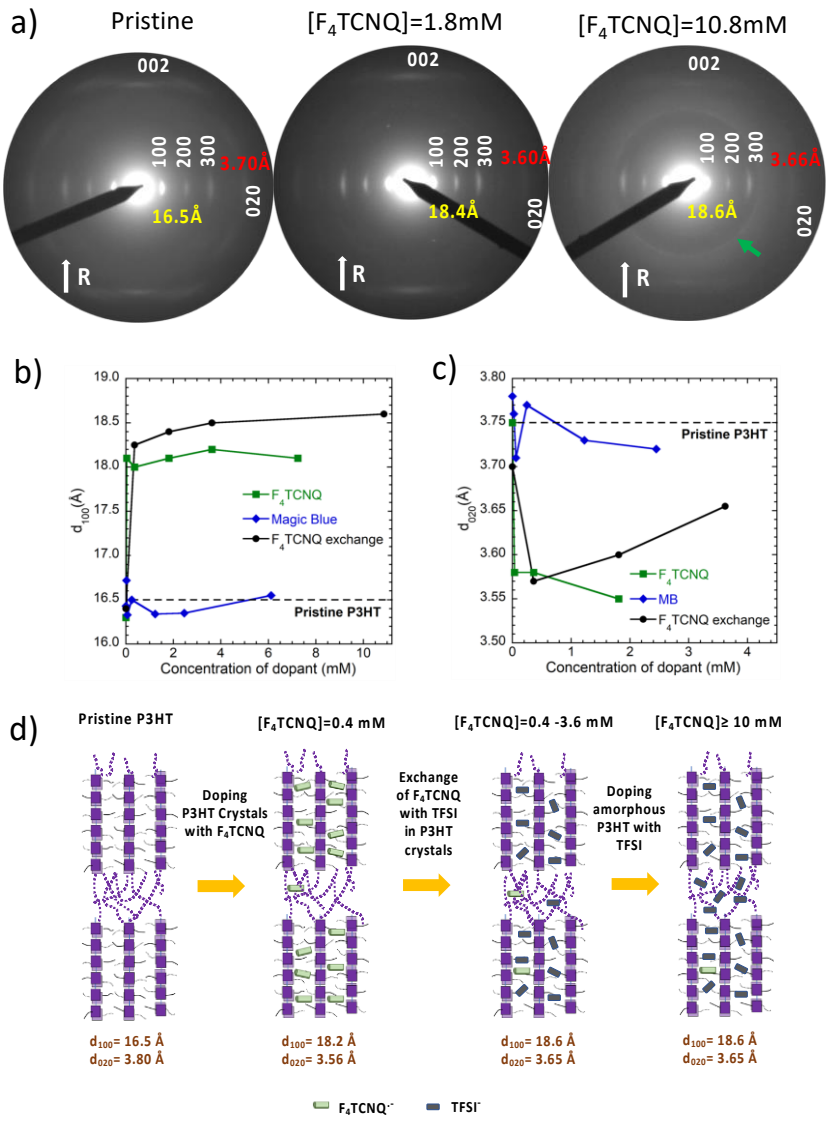

Figure 3. *a) Typical electron diffraction patterns of oriented P3HT in pristine state (a) and after ICAED for two different concentrations. The main reflections are indexed and corresponding reticular distances are shown. The green arrow points at a Scherrer ring related to the overlayer formed atop the doped P3HT film (see text). b) and c) Evolution of lattice parameters* d_{100} *and* d_{020} *(*π*-stacking) as a function of [*F_4*TCNQ] concentration in the blends with LiTFSI, respectively. The data for films doped with magic blue and pure* F_4*TCNQ are retrieved from ref. 13 and 7, respectively. d) Schematic illustration of the anion exchange doping mechanism as a function of increasing concentration in solution of* F_4*TCNQ/LiTFSI.*

Accordingly, the TEM data confirm the results gained from UV-vis-NIR spectroscopy i.e. the existence of two regimes of doping: i) a first regime at [F_4TCNQ] ≤1.8 mM/l dominated by the presence of F_4TCNQ^- in the P3HT crystals and ii) a second regime for a concentration above 2 mM for which $TFSI^-$ replaces F_4TCNQ^- in the crystals and dopes further the amorphous phase of P3HT (see **Figure 3.c**). At this high level of doping, the ED pattern also displays a diffuse Scherrer ring. It is attributed to the presence of an ionic-liquid like layer made of F_4TCNQ/LiTFSI mixture in n-BA that recovers the doped P3HT films. As demonstrated by POM, only upon slow drying over 1 day are the droplets replaced by some crystals corresponding to excess of F_4TCNQ/LiTFSI and LiF_4TCNQ (see **Figure S2**).

Thermoelectric properties. The evolution of the thermoelectric properties i.e. charge conductivity and thermopower reflect the spectroscopic and structural changes upon ICAED. They are depicted in **Figure 4**. First, the charge conductivity is highly anisotropic as for other dopants with a ratio $\sigma_{//}/\sigma_{\perp}$ in the range 8.4-13.8 and there is some anisotropy of the Seebeck coefficient ($S_{//}/S_{\perp}$ in the range 2.4-3.0).[32] The conductivity in the chain direction increases to a maximum value of $3.0\pm0.4\cdot10^3$ S/cm for 21.7 mM whereas the Seebeck coefficient retains a value of 23 μV/K leading to a thermoelectric power factor of 164±20 μW/mK^2. These values are close to those reported for P3HT doped with magic blue. The power factor is similar to that reported for oriented P3HT doped with $Mo(tdfCOCF_3)_3$ (see **Figure 4.d**).

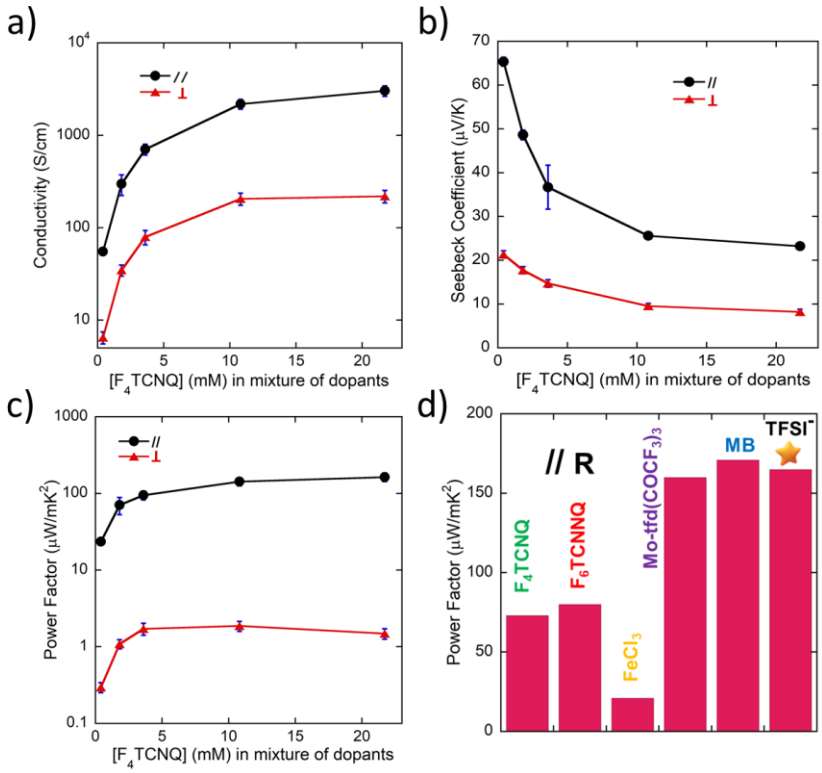

Figure 4. *Evolution of anisotropic charge conductivity (a), Seebeck coefficient (b) and power factor (c) as a function of the concentration of F_4TCNQ in the blend with LiTFSI (1:5 ratio in n-BA) measured parallel and perpendicular to the rubbing direction. d) Maximum power factors for various dopants of oriented P3HT films (taken from literature) as measured in the chain direction.*

As compared to F_4TCNQ-doped P3HT, a much higher oxidation is achieved by anion exchange with TFSI leading to this substantial increase in PF from 56 $\mu W/m{\cdot}K^2$ to 164 $\mu W/m{\cdot}K^2$. In principle, it might be possible to further dope the P3HT films to stronger levels as no sign of saturation of the charge conductivity is seen upon increasing the concentration of F_4TCNQ/LiTFSI up to 21.7 mM. The formation of an overlayer of an ionic liquid -like solution (LiTFSI+ F_4TCNQ+ ACN) on top of the films precludes, however, the use of higher concentrations of dopant mixtures.

Overall, the final thermoelectric performances for P3HT films doped by ICAED are close to those observed for P3HT doped with magic blue. So far, the highest power factors for doped and oriented P3HT seem to plateau at a value in the range 150-170 $\mu W/m \cdot K^2$ regardless of the type of dopant. However, the structure analysis by TEM shows that $TFSI^-$ molecules are present in the unit cell of P3HT. Thus, the crystal structure of P3HT is modified upon doping whereas for MB-doped films the dopant molecules are exclusively located in the amorphous phase (see the lattice parameter variation *versus* dopant concentration in **Figure 3**). Unexpectedly, the final conductivities reached in both $TFSI^-$-exchanged and MB-doped P3HT are similar despite different locations of dopants in the polymer matrix. However, as seen now, the different location of the dopant in the polymer microstructure has a strong impact on the stability of the doped P3HT films.

2) Stability and ageing of oriented and doped P3HT films.

Applications in thermoelectricity require long-term stability of the materials. So far, very few studies have addressed this important issue.[30,33,34] In this contribution, we underline the differences in stability between MB-doped and $TFSI^-$-exchanged rub-aligned P3HT. As stated above, the choice of these two systems is justified by the fact that dopants are not located in the same way in the P3HT polymer matrix. For this purpose, we follow the stability of the doped polymers stored in a glovebox in the dark for up to 50 days. We measure the evolution of the charge conductivity and the Seebeck coefficient versus ageing time as well as corresponding changes in the polarized UV-vis-NIR spectra. **Figure 5** shows the evolution of the polarized UV-vis-NIR spectrum measured along and perpendicular to the chain direction for films doped with magic blue or with TFSI.

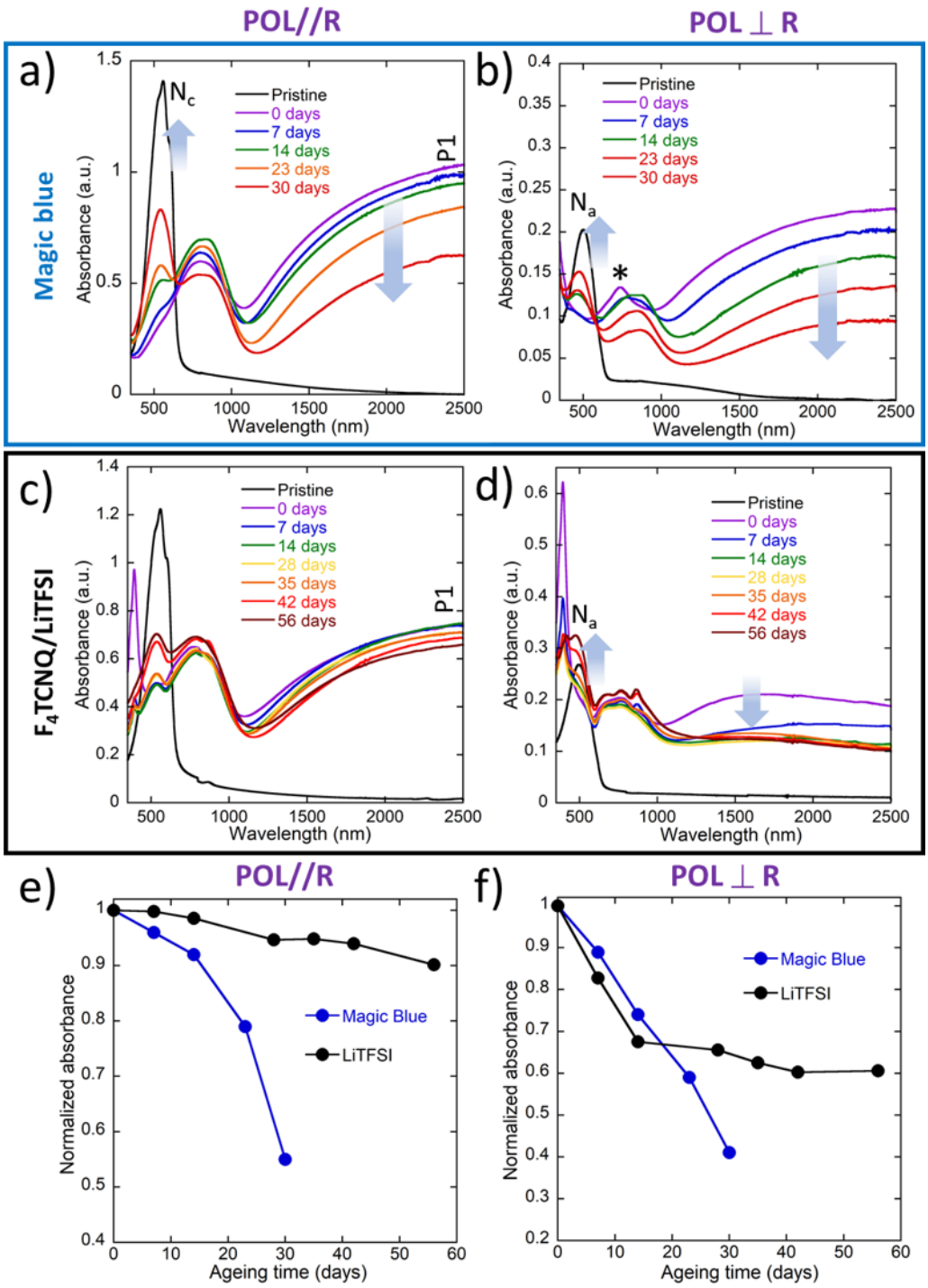

Figure 5. *Evolution of the UV-vis-NIR spectra of oriented P3HT doped either with magic blue (a and b) or by ICAED using F_4TCNQ/LiTFSI (c and d) upon ageing in an inert atmosphere without light. The spectra are recorded for the light polarization parallel (a and c) and perpendicular (b and d) to the rubbing direction. N_a designates the neutral absorption band of amorphous P3HT and N_c the crystalline P3HT one. e) and f) corresponding evolution of the*

normalized absorbance of the P1 band (2500nm) of MB-doped and $TFSI^-$-exchanged *films of oriented P3HT recorded for the light polarized parallel (e) or perpendicular (f) to the rubbing direction.*

De-doping of the crystalline or the amorphous phases can be followed by selecting the light polarization (POL//R for crystalline and POL⊥R for amorphous). Following the loss in absorbance of polaronic bands is a means to follow the loss of charge carriers. We want to emphasize that the purpose of this study is not to identify the chemical or physical (e.g. diffusion) mechanism responsible for the de-doping of the films upon ageing but to highlight the correlation between time-scale of de-doping and location of dopants in the polymer matrix.

De-doping is characterized by the loss of absorbance of polaronic bands and a corresponding increase of the neutral polymer absorption. As seen in **Figure 5**, TFSI- and MB-doped films show different de-doping trends. In the case of MB-doped P3HT, we observe that the polaronic band P1 shows a very strong decrease in absorption for both polarization directions whereas the neutral absorption bands of crystalline (N_c) and amorphous (N_a) P3HT increase substantially (**Figure 5.a** and **5.b**). The final absorbance of the P1 band is in the range 40-50% of the original value after 30 days ageing. This observation indicates that both crystalline and amorphous P3HT de-dope strongly over a time period of 30 days in the dark and under inert atmosphere.

$TFSI^-$-exchanged P3HT has a very different behavior. For POL⊥R, the polaronic P1 band decreases very substantially and saturates to approx. 60% of the initial value whereas the neutral absorption band of amorphous P3HT increases at the same time. This indicates partial de-doping of amorphous zones of P3HT. For POL//R, the loss in absorbance of P1 is much more reduced (about 10%) even after 56 days, suggesting that de-doping of crystalline P3HT is less important than in the case of MB. Even when stored under inert atmosphere and in the

dark, doped P3HT films do indeed lose polaronic species upon ageing over a time scale of 30-40 days, but some stabilization is provided by the method of ICAED . Let us see now how the change in polaron populations affects charge conductivity.

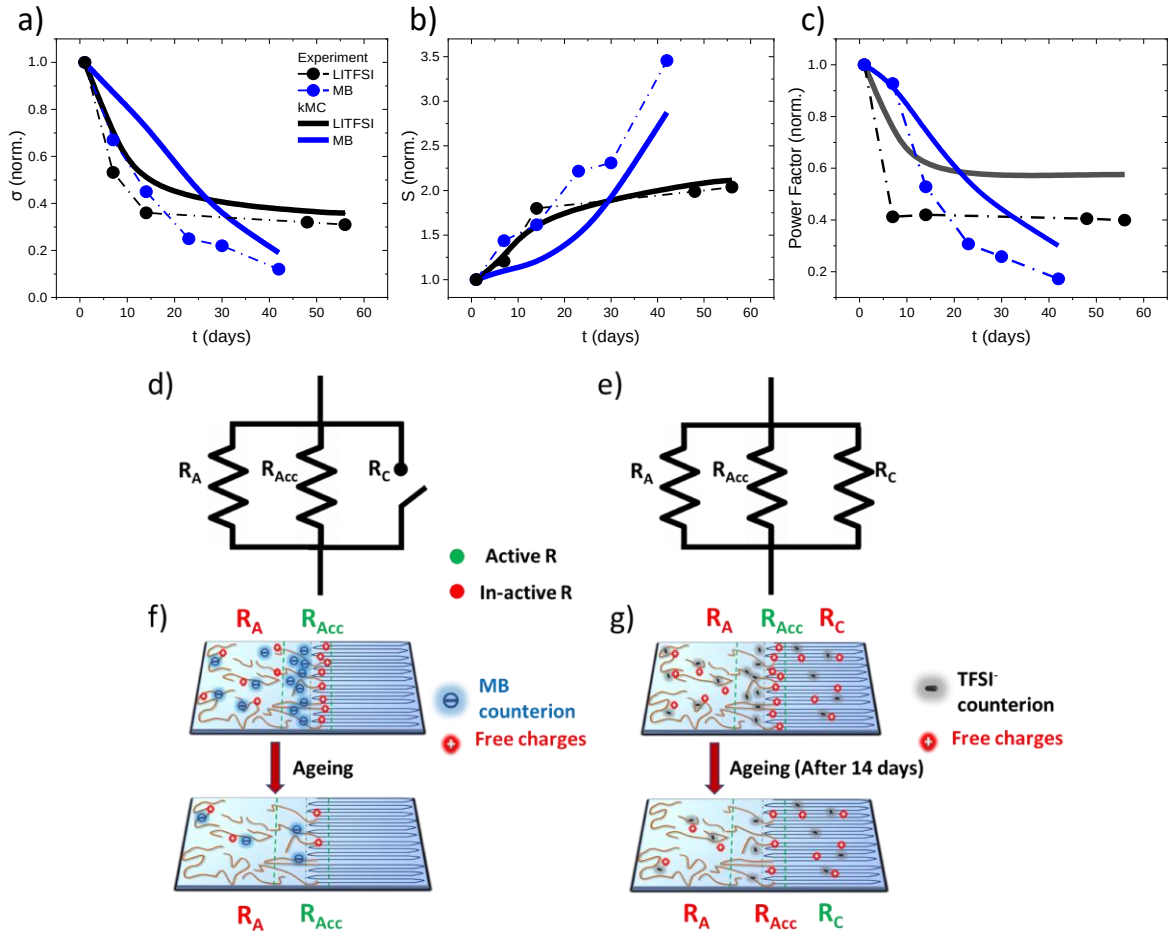

Figure 6. *Figure 1. kMC simulated (a) conductivity, (b) Seebeck coefficient and (c) power factor versus ageing time, compared with the experiments for MB-doped and TFSI-exchanged aligned P3HT. Illustration of relevant channels for charge transport in (d) MB- and (e) TFSI⁻-exchanged P3HT by a parallel resistance model. (f, g) Schematics illustrating the charge distribution in different channels. In green, the dominant channel in charge transport is indicated, before and after ageing in (f) MB-doped and (g) TFSI⁻-exchanged P3HT. The standard set of VRH model parameters used:* ΔE_{HOMO}*=0.3 eV, A:C-45:55 for i) TFSI -exchanged (black line):* $\sigma_{dos,C}$*=55 meV* $\sigma_{dos,A}$*=85 meV,* D_A*:*D_C *- 70:30 ii) MB-doped (Blue):*

$\sigma_{dos,C}$=45 meV $\sigma_{dos,A}$=75 meV, D_A:D_C - 100:0. σ_{dos} gradually increases by up to 1k_BT with ageing, until reaching maximum ageing.

Figures 6.a-b depict the normalized conductivity variation ($\sigma_{//}(t)/\sigma_{//}(t=0)$), Seebeck coefficient and power factor as a function of ageing time for MB-doped and $TFSI^-$-exchanged P3HT films. In the case of magic blue, the charge conductivity of the films drops to 12% of the original value after 42 days in the chain direction whereas the drop is smaller perpendicular to the rubbing, see **Figures S3** and **S4**. The relative conductivity variations probed parallel ($\Delta\sigma_{//}$) and perpendicular ($\Delta\sigma_{\perp}$) to the rubbing show a linear correlation (**Figure S4**). This is consistent with the fact that MB dopants located in the amorphous phase dope both crystals and amorphous phases through the accumulation layer at their interface, hence, both phases should de-dope in a similar manner. The conductivity did not decrease proportionally to the P1 band absorbance and there is no linear relation between P1 band absorbance and conductivity (**S6**). This is not surprising since de-doping implies possibly two mechanism occurring in parallel: bipolaron → polaron and polaron → neutral. The decrease of normalized conductivity with ageing time could be fitted to a simple exponential decay such as $\sigma_{//,\perp}(t)= \sigma_{//,\perp}(0)\cdot\exp(-t/\tau)+ \sigma_{//,\perp}(\infty)$ with a typical time constant τ and introducing also a plateau conductivity $\sigma_{//,\perp}(\infty)$. **Table S1** collects the characteristic decay times τ and the plateau values. Such exponential decay is compatible with a chemical reaction involving for instance the degradation of the counter-ions upon reaction with trace amounts of water in the glovebox.[34]

By contrast, in $TFSI^-$-exchanged films, the charge conductivity tends to plateau to 31% of the original conductivity in inert condition (dark). The ageing of the thermoelectric power factor reveals the same trend: a leveling to 40% of the initial PF value. Even in ambient condition (dark), a saturation of the power factor is observed, albeit at a lower value (see **Figure S5**). At this point, it is worth to highlight that the different stabilities of MB-doped and $TFSI^-$-

exchanged films may relate to different degradation mechanisms linked with the chemical natures of the counterions present in the films ($SbCl_6^-$ versus $TFSI^-$).[34] It was proposed that the hydrophobic character of TFSI helps avoid reductive reactions with H_2O in poly(3-octylthiophene) thin films, explaining the longer lifetime of doped P3HT films.

Further insight into the ageing process can be obtained from the evolution of the Seebeck coefficient, or more precisely, from the correlation between Seebeck coefficient and charge conductivity.[35-37] As noted in our previous work, anisotropic charge transport phenomena in doped PSCs can be analyzed by following the S-σ correlations.[13,37] In the case of rub-aligned films, different scaling laws are observed in the directions parallel and perpendicular to the polymer chain direction.[13] Moreover, for a given polymer, these scaling laws are essentially independent of the chemical nature of the dopant. [13,5] In Figure S7, we plotted the S-σ correlations for rub-aligned P3HT in the chain direction doped with various dopants along with the scaling law $S \propto \sigma^{-1/4}$. The S-σ data points corresponding to ageing are added to this master curve for MB and TFSI-exchanged P3HT films. For TFSI-exchanged films, ageing produces samples such that the S,σ points fall onto the expected master curve, suggesting that de-doping is a reversible mechanism that does not alter the intrinsic transport properties of the oriented P3HT. For MB-doped films the situation is different. Upon dedoping, S,σ points tend to deviate from the master curve, suggesting an irreversible de-doping mechanism that fundamentally affects transport in the MB-doped P3HT films. This is a very interesting result, suggesting that scrutinizing S-σ correlations can help distinguish reversible and irreversible ageing processes in doped PSC films.

3) Kinetic Monte Carlo (kMC) simulations of doped P3HT ageing.

To investigate the dopant-dependent thermoelectric stability of the polymer, we use numerically exact kinetic Monte Carlo (kMC) simulations for variable-range hopping of charges on a cubic lattice. The simulation morphology distinguishes ordered (C: aggregates/crystalline) and amorphous phases (A) in a phase volume ratio A:C. The difference in microstructure between the phases results in an offset in HOMO levels by ΔE_{HOMO} [38,39] and different energetic disorder (σ_{dos}) for each phase. In addition, the model accounts for the preferential positioning of the dopants (D_A:D_C) in different phases of the polymer. Importantly, to replicate the ageing phenomenon, we de-dope the amorphous and crystalline phases in the model based on the experimentally observed decay in absorbance of the P1 band with ageing time, as illustrated in **Figure 5.e-f.** Further details about the model are provided in Ref. 14.

Figure 6.a and **6.c** depict a monotonous and non-saturating decrease in conductivity and power factor with ageing for the MB dopant, while the LITFSI dopant does show a pronounced saturation/stabilization with ageing time. Both results quasi-quantitatively match the experiments. Additionally, the shorter half-life of $TFSI^-$-exchanged material compared to the MB-doping is reproduced.

To comprehend the above phenomena, we first need to identify the relevant transport channels depending on the location of the dopants in the polymer. Based on our previous work, we can simplify the understanding of the overall charge transport using a parallel channel resistance model, provided there is a long-range interconnection among phases in the polymer film. In our case, MB and $TFSI^-$ primarily reside in the amorphous phase, which leads to the formation of an accumulation layer on the ordered side of the interface between the two phases. This spontaneous modulation doping is driven by the balance between the energy gain ΔE_{HOMO} associated with moving mobile holes to the ordered phase and the (electrostatic) energy loss associated with separating holes from their counter ions.[14] Additionally, a minor fraction of $TFSI^-$ counter-ions enters the crystalline phase during the ion-exchange. Hence, as depicted in

Figure 6.d and **6.e**, only the resistances of the amorphous and accumulation phases are relevant for MB, whereas for LITFSI, the crystalline phase also stays relevant for the overall charge transport. The resistance (R) of these phases can be determined by their respective carrier density (n) and mobility (μ), expressed as $R \propto \frac{1}{n\mu}$.[40] For a given carrier density, the phase mobility is influenced by both the phase crystallinity[41] and the presence of scattering centers[42] in the form of dopant counter-ions within that phase.

Importantly, during the ageing process, the different channel resistances get changed in different ways, depending on the varying rate of charge depletion from each phase, as depicted in **Figure 6**. For MB, the de-doping of the amorphous phase leads to an additional depletion of charges from the accumulation layer. Since the accumulation layer sits in the high(er) crystallinity phase and is spatially separated from the ionic scattering centers, the associated resistance (R_{Acc}) dominates the overall charge transport throughout the entire ageing time, as illustrated in **Figure 6.f**. Along the same line, at short aging times, charge transport for $TFSI^-$-exchanged materials is dominated by the accumulation layer. However, once the accumulation layer is sufficiently depleted (by the escape of the counter ions from the amorphous phase), the remaining concentration of ions in the crystalline phase makes that the resistance of the crystalline phase (R_C) becomes dominant. In other words, the benefit of reduced Coulomb interaction, due to the absence of scattering centers in the (interfacial) accumulation layer, is surpassed by the higher (bulk) charge carrier in the crystalline phase, as depicted in **Figure 6.g**. The dominance of the crystalline phase resistance leads to the retention of the overall film conductivity after several weeks, and at the same time the non-zero conductivity at very long ageing times.

The quick initial decay in conductivity, and hence a shorter half-life, is due to the strong charge drop in the accumulation phase for $TFSI^-$, as compared to the MB doped case. This is in response to the stronger de-doping occurring in the amorphous phase for $TFSI^-$ until 14 days,

as depicted in **Figure 6**. The higher diffusion constant of small-sized counter-ions, such as $TFSI^-$ ions, may lead to a quicker diffusion of counter-ions out of the film, hence destabilizing the accumulation phase, as compared to the larger MB dopant.[43-45,5]

To conclude, the retention of charges in any phase appears to be crucial for the stability in conductivity, whereas the specific phase capable of retaining the charge, quantitatively determines the conductivity at long ageing times, σ_∞. As such, and counter-intuitively, charge retention in the amorphous phase can provide the highest σ_∞ due to the accumulation layer remaining intact. When the doping level in the amorphous phase is unstable (MB), it is beneficial to have a significant and stable doping level in the crystalline phase as observed for $TFSI^-$-exchanged films. This interesting result suggests that the way the microstructure of a semi-crystalline polymer is doped impacts the long-term stability of its TE properties.

Conclusion.

Incremental concentration anion exchange doping can progressively dope oriented P3HT films. The mechanism of anion exchange between $F_4TCNQ^{\cdot-}$ and $TFSI^-$ is determined by the concentration of dopant and three steps are observed. At low concentration of F_4TCNQ/LiTFSI ($[F_4TCNQ] \leq 3.6$ mM), P3HT crystals are mainly doped by F_4TCNQ and the amorphous phase is undoped. Above a threshold concentration of 3.6 mM, anion exchange takes place and $TFSI^-$ replaces F_4TCNQ^- in the P3HT crystals. Finally, once crystals are saturated with $TFSI^-$, diffusion to and doping of amorphous zones of the polymer takes place. The resulting TE performances of $TFSI^-$-exchanged and oriented P3HT are at the same level as for the dopants magic blue and $Mo(tdfCOCF_3)_3$ with charge conductivities of the order of 3000 S/cm and a PF beyond 150 $\mu W/mK^2$. However, even under inert atmosphere, MB-doped films are unstable and both charge conductivity and PF are fully lost within 30 days ageing time in a glovebox

and in the dark. In strong contrast, $TFSI^-$-exchanged P3HT reaches a stabilized PF value of 40% of its original value after 56 days storage in a glovebox.

The different ageing kinetics are attributed to the differences in the way dopants are initially inserted in the semi-crystalline structure of the polymer. $TFSI^-$-exchanged P3HT films are more stable towards de-doping because dopants are present in both crystalline and amorphous zones. Despite de-doping of the amorphous zones, transport properties are retained in $TFSI^-$-exchanged films since $TFSI^-$ counterions stay over long time in P3HT crystals. The excellent charge transport in MB-doped films arise from the presence of the accumulation layer at the crystal/amorphous interface but the instability of doping in the amorphous phase results in a fast drop of transport properties. Overall, this work underlines the necessity to better control the relation between polymer microstructure (semi-crystallinity or liquid crystal-like structure) and doping in order to ensure long-term stability of doped PSCs.

Acknowledgments.

Bernard Lotz is gratefully acknowledged for fruitful discussions and careful reading of the manuscript. M. Schmutz is acknowledged for technical support with TEM. N. Zimmermann is acknowledged for technical support in pre-patterned device preparation. Financial support from ANR grant Thermopolys is acknowledged. This work was financially supported by the European Commission through Marie Sklodowska-Curie project HORATES (GA-955837). M.K. thanks the Carl Zeiss Foundation for financial support.

Conflict of interest.

The authors declare no conflict of interest.

IV. Experimental section.

Materials and oriented film preparation.

Regio-regular P3HT was purchased from Ossila (M_w = 60.15 kDa, M_n=28.65 kDa and DI=2.1, RR=97.6%). F_4TCNQ and LiTFSI (Lithium bis(trifluoromethanesulfonyl)imide) were purchased from TCI. Magic Blue, anhydrous solvents (99%) used for doping (acetonitrile, n-butylacetate(n-BA)) and film preparation (ortho-dichlorobenzene) as well as sodium poly(styrenesulfonate) (NaPSS) were purchased from Sigma Aldrich. Following a procedure outlined in previous publications[7,13], P3HT films were deposited via doctor blading from a 15g/l solution in ODCB at 154°C on glass substrates covered with a sacrificial layer of NaPSS. The NaPSS layer was spin-coated at 3000 RPM from 10g/l aqueous solution on glass substrates cleaned by ultrasonication in acetone, ethanol, hellmanex and deionized water (3 times). Rub-alignment was performed using a homemade setup involving a rotating cylinder covered with a microfiber cloth and a translating hot stage. Film thickness was determined from UV-Vis absorbance using a calibration provided in reference 46.

Doping protocols.

The doping process of P3HT films with Magic Blue (MB) followed the ICD protocol, involving complete immersion of the samples for 45-60 seconds in an acetonitrile solution of increasing concentration. Anion exchange doping was carried out by immersing the P3HT films in a mixture of F_4TCNQ and LiTFSI (at a 1:5 ratio (g/L) in n-butyl acetate) at 70°C for 15 minutes. Incremental concentration anion exchange doping (ICAED) was conducted by sequentially dipping the films in solutions of increasing doping concentration. The final concentration (21.7 mM F_4TCNQ+ 104.5 mM LiTFSI) and ratio of the dopant mixtures in n-butyl acetate were adopted from reference 17. The dopant ratio in the solution and other doping conditions were consistently maintained for each concentration. In contrast to reference 19.b, to prevent de-doping of the films, the doped films were not rinsed with the pure solvent, resulting in some

overlayer of dopant in n-butyl acetate for the highest doping concentrations (see **Figure S2**). Both the doping and rubbing processes were performed in a Jacomex glovebox.

Structural analysis by TEM.

Oriented P3HT films were coated with a thin amorphous carbon film using an Edwards Auto306 evaporator. Subsequently, the films were floated on distilled water and transferred onto TEM copper grids. The same doping conditions identified for spectroscopy and transport measurements were applied to dope the grids (MB and $TFSI^-$). After removing the excess dopant solution by blotting, grids were transferred into the TEM sample holder. The samples were only swiftly exposed to air (10–20 s) just before introducing the sample holder into the vacuum of the TEM. For electron diffraction (ED) analysis before and after doping, a CM12 Philips microscope (120 kV) equipped with an MVIII (Soft Imaging System) camera was utilized. Beam exposure was minimized (low dose system) to avoid de-doping of the oriented films under the electron beam, when the same zone is exposed for a prolonged period of time. The 0 0 2 reflection at 3.75 Å is insensitive to doping and was therefore used as an internal calibration reference to calculate the d_{100} and d_{020} reticular distances in the ED patterns.

Polarized UV–Vis–NIR Absorption.

A Cary 5000 spectrometer with spectral resolution of 1 nm and polarized incident light was used to probe the UV−vis−NIR absorption (350−2500 nm) of the oriented polymer films as a function of doping. The spectra were recorded with incident light polarization (POL) parallel or perpendicular to the rubbing (0° corresponding to POL//R and 90° to POL⊥R).

FTIR spectroscopy.

Fourier Transform Infrared (FTIR) spectra were acquired using a Bruker Vertex 70 spectrometer with a resolution of 2 cm^{-1}. Oriented P3HT films were transferred onto precleaned Si(100) substrates. Cleaning was performed using ultrasonicating with acetone, ethanol, hellmanex and deionized water (x2 times). Following wet-cleaning the substrates were dried

thoroughly at 120°C followed by treatment with a UV ozone cleaner . Films were doped as per ICAED protocol and measured using DTGS transmission mode ranging from 7500 cm^{-1} to 370 cm^{-1}. Each spectrum is the average of 100 spectra. Correction for H_2O and CO_2 was performed for each spectrum.

Charge Conductivity and Seebeck Coefficient.

Cleaned glass substrates were dried under nitrogen and treated with plasma prior to electrode deposition. Gold electrical contacts, 40 nm thick, were deposited in a four-points probe configuration (1 mm spacing between electrodes, 5 mm length) using high vacuum thermal evaporation through a shadow mask at a deposition rate of 4–6 Å/s. A 2.5 nm thick Chromium layer was first deposited to enhance adhesion to the glass substrates (evaporation rate 0.5-1 Å/s). Two electrode devices were aligned parallel to each other, and two were oriented perpendicular to the rubbing direction on the same substrate. The oriented films were meticulously cut to match the size of the device-substrate and then floated on distilled water. They were subsequently positioned on the glass substrates with electrode patterns, ensuring correct alignment of the electrode orientation with the film rubbing direction. Doping was performed using the ICD protocol for MB doping and ICAED protocol for $TFSI^-$ doping.

All assessments of electrical conductivity and Seebeck coefficient were carried out in a Jacomex glovebox under an N_2 atmosphere with $PO_2 \leq 2$ ppm and $PH_2O \leq 1$ ppm. Electrical conductivity was measured using a Keithley 2436b and a Semiprobe station (Lab assistant 150). The conductivity (σ) was deduced from the resistance R using the relationship $\sigma = 1/(1.81.R.t)$, where 't' denotes the film thickness.[47] The film thickness was determined via UV-vis absorbance, with calibration conducted using the reference provided in reference 46 for P3HT. The thermopower was measured using a differential temperature method whereby a temperature gradient was established across the sample along or perpendicular to the rubbing direction. The temperature gradient was ramped between 0 and 12K around room temperature

and the Seebeck coefficient was extracted by plotting the thermovoltage *versu*s temperature gradient. A constantan wire was used to calibrate the Seebeck coefficient. The detailed procedure is given in reference 47. Data analysis and fitting were performed using Kaleidagraph.

Stability measurements.

Stability testing was performed under inert atmosphere (glovebox) in the dark for doped P3HT samples (MB and $TFSI^-$) over a period of 30-60 days. Periodic measurements of polarized UV-Vis-NIR spectra and thermoelectric parameters were conducted at seven-day intervals.

References.

1) A. D. Scaccabarozzi, A. Basu, F. Aniés, J. Liu, O. Zapata-Arteaga, R. Warren, Y. Firdaus, M. I. Nugraha, Y. Lin, M. Campoy-Quiles, N. Koch, C. Müller, L. Tsetseris, M. Heeney and T. D. Anthopoulos, *Chem. Rev.*, 2022, **122**, 4420–4492.
2) I. E. Jacobs and A. J. Moulé, *Advanced Materials*, 2017, **29**, 1703063
3) I. E. Jacobs, E. W. Aasen, J. L. Oliveira, T. N. Fonseca, J. D. Roehling, J. Li, G. Zhang, M. P. Augustine, M. Mascal and A. J. Moulé, *J. Mater. Chem. C*, 2016, **4**, 3454–3466.
4) E. Lim, K. A. Peterson, G. M. Su and M. L. Chabinyc, *Chem. Mater.*, 2018, **30**, 998–1010.
5) V. Vijayakumar, P. Durand, H. Zeng, V. Untilova, L. Herrmann, P. Algayer, N. Leclerc and M. Brinkmann, *J. Mater. Chem. C*, 2020, **8**, 16470–16482.
6) R. Kroon, D. A. Mengistie, D. Kiefer, J. Hynynen, J. D. Ryan, L. Yu and C. Müller, *Chem. Soc. Rev.*, 2016, **45**, 6147–6164.
7) V. Untilova, H. Zeng, P. Durand, L. Herrmann, N. Leclerc and M. Brinkmann, *Macromolecules*, 2021, **54**, 6073–6084.
8) S. Guchait, L. Herrmann, K. Kadri, N. Leclerc, F. Tran Van, M. Brinkmann, *ACS Appl Polym Mater*, 2023, **5**, 5676.
9) E. F. Aziz, A. Vollmer, S. Eisebitt, W. Eberhardt, P. Pingel, D. Neher and N. Koch, *Advanced Materials*, 2007, **19**, 3257–3260.
10) K. Tashiro, M. Kobayashi, T. Kawai and K. Yoshino, *Polymer*, 1997, **38**, 2867–2879.

11) M. Comin, V. Lemaur, A. Giunchi, D. Beljonne, X. Blase and G. D'Avino, *J. Mater. Chem. C*, 2022, **10**, 13815–13825.

12) A. I. Hofmann, R. Kroon, S. Zokaei, E. Järsvall, C. Malacrida, S. Ludwigs, T. Biskup and C. Müller, *Advanced Electronic Materials*, 2020, **6**, 2000249.

13) Y. Zhong, V. Untilova, D. Muller, S. Guchait, C. Kiefer, L. Herrmann, N. Zimmermann, M. Brosset, T. Heiser and M. Brinkmann, *Advanced Functional Materials*, 2022, **32**, 2202075.

14) A. Dash, S. Guchait, D. Scheunemann, V. Vijayakumar, N. Leclerc, M. Brinkmann, M. Kemerink, *Advanced Materials*, ***n/a***, 2311303.

15) V. Vijayakumar, Y. Zhong, V. Untilova, M. Bahri, L. Herrmann, L. Biniek, N. Leclerc and M. Brinkmann, *Advanced Energy Materials*, 2019, **9**, 1900266.

16) E. M. Thomas, K. A. Peterson, A. H. Balzer, D. Rawlings, N. Stingelin, R. A. Segalman and M. L. Chabinyc, *Advanced Electronic Materials*, 2020, **6**, 2000595.

17) Y. Yamashita, J. Tsurumi, M. Ohno, R. Fujimoto, S. Kumagai, T. Kurosawa, T. Okamoto, J. Takeya and S. Watanabe, *Nature*, 2019, **572**, 634–638.

18) Y. Yamashita, J. Tsurumi, T. Kurosawa, K. Ueji, Y. Tsuneda, S. Kohno, H. Kempe, S. Kumagai, T. Okamoto, J. Takeya and S. Watanabe, *Communications Materials*, 2021, **2**, 45.

19) a) I. E. Jacobs, Y. Lin, Y. Huang, X. Ren, D. Simatos, C. Chen, D. Tjhe, M. Statz, L. Lai, P. A. Finn, W. G. Neal, G. D'Avino, V. Lemaur, S. Fratini, D. Beljonne, J. Strzalka, C. B. Nielsen, S. Barlow, S. R. Marder, I. McCulloch and H. Sirringhaus, *Advanced Materials*, 2022, **34**, 2102988. b) Y. Huang, D. H. Lukito Tjhe, I. E. Jacobs, X. Jiao, Q. He, M. Statz, X. Ren, X. Huang, I. McCulloch, M. Heeney, C. McNeill, H. Sirringhaus, *Appl. Phys. Lett.* **2021**, *119*, 111903.

20) T. L. Murrey, M. A. Riley, G. Gonel, D. D. Antonio, L. Filardi, N. Shevchenko, M. Mascal and A. J. Moulé, *J. Phys. Chem. Lett.*, 2021, **12**, 1284–1289.

21) J. Hynynen, D. Kiefer and C. Müller, *RSC Adv.*, 2018, **8**, 1593–1599.

22) J. Hynynen, D. Kiefer, L. Yu, R. Kroon, R. Munir, A. Amassian, M. Kemerink and C. Müller, *Macromolecules*, 2017, **50**, 8140–8148.

23) I. E. Jacobs, G. D'Avino, V. Lemaur, Y. Lin, Y. Huang, C. Chen, T. F. Harrelson, W. Wood, L. J. Spalek, T. Mustafa, C. A. O'Keefe, X. Ren, D. Simatos, D. Tjhe, M. Statz, J. W. Strzalka, J.-K. Lee, I. McCulloch, S. Fratini, D. Beljonne and H. Sirringhaus, *J. Am. Chem. Soc.*, 2022, **144**, 3005–3019.

24) Y. He, N. A. Kukhta, A. Marks and C. K. Luscombe, *J. Mater. Chem. C*, 2022, **10**, 2314–2332.

25) M. Goel and M. Thelakkat, *Macromolecules*, 2020, **53**, 3632–3642.

26) D. Kiefer, R. Kroon, A. I. Hofmann, H. Sun, X. Liu, A. Giovannitti, D. Stegerer, A. Cano, J. Hynynen, L. Yu, Y. Zhang, D. Nai, T. F. Harrelson, M. Sommer, A. J. Moulé, M. Kemerink, S. R. Marder, I. McCulloch, M. Fahlman, S. Fabiano and C. Müller, *Nature Materials*, 2019, **18**, 149–155.

27) A. Hamidi-Sakr, L. Biniek, S. Fall and M. Brinkmann, *Advanced Functional Materials*, 2016, **26**, 408–420.

28) S. Guchait, Y. Zhong and M. Brinkmann, *Macromolecules*, 2023, **56**, 6733–6757.

29) O. Zapata-Arteaga, B. Dörling, A. Perevedentsev, J. Martín, J. S. Reparaz and M. Campoy-Quiles, *Macromolecules*, 2020, **53**, 609–620

30) K. E. Watts, B. Neelamraju, E. L. Ratcliff and J. E. Pemberton, *Chem. Mater.*, 2019, **31**, 6986–6994.

31) $\delta = 2\Delta\nu/\nu_o[1-(\nu_1/\nu_o)^2]^{-1}$ with ν_o and ν_1 the vibrational frequencies for the neutral and the charged molecules at 2227 cm^{-1} and 2194 cm^{-1}, respectively. For more details, see the reference: M. Meneghetti and C. Pecile, *The Journal of Chemical Physics*, 1986, **84**, 4149–4162.

32) D. Scheunemann, V. Vijayakumar, H. Zeng, P. Durand, N. Leclerc, M. Brinkmann, M. Kemerink, *Advanced Electronic Materials* **2020**, *6*, 2000218.

33) M. Craighero, J. Guo, S. Zokaei, S. Griggs, J. Tian, J. Asatryan, J. Kimpel, R. Kroon, K. Xu, J. S. Reparaz, J. Martín, I. McCulloch, M. Campoy-Quiles and C. Müller, *ACS Appl. Electron. Mater.*, 2023, DOI:10.1021/acsaelm.3c00936.

34) J.-L. Ciprelli, C. Clarisse and D. Delabouglise, *Synthetic Metals*, 1995, **74**, 217–222.

35) S. D. Kang, G. J. Snyder, *Nature Materials* **2016**, *16*, 252.

36) S. A. Gregory, R. Hanus, A. Atassi, J. M. Rinehart, J. P. Wooding, A. K. Menon, M. D. Losego, G. J. Snyder, S. K. Yee, *Nature Materials* **2021**, *20*, 1414.

37) P. Limelette, N. Leclerc, M. Brinkmann, *Scientific Reports* **2023**, *13*, 21161.

38) C. Groves, *Energy & Environmental Science*, 2013, **6**, 1546.

39) W. C. Tsoi, S. J. Spencer, L. Yang, A. M. Ballantyne, P. G. Nicholson, A. Turnbull, A. G. Shard, C. E. Murphy, D. D. C. Bradley, J. Nelson, J.-S. Kim, *Macromolecules*, 2011, **44**, 2944.

40) A. Dash, D. Scheunemann, M. Kemerink, *Phys. Rev. Appl.*, 2022, **18**, 064022.

41) D. T. Scholes, P. Y. Yee, G. R. McKeown, S. Li, H. Kang, J. R. Lindemuth, X. Xia, S. C. King, D. S. Seferos, S. H. Tolbert, B. J. Schwartz, *Chem. Mater.*, 2019, **31**, 73.

42) G. Zuo, H. Abdalla, M. Kemerink, *Phys. Rev. B*, 2016, **93**, 235203.

43) T. Nishida, K. Nishikawa, Y. Fukunaka, *ECS Trans.*, 2008, **6**, 1.

44) J. Li, C. Koshnick, S. O. Diallo, S. Ackling, D. M. Huang, I. E. Jacobs, T. F. Harrelson, K. Hong, G. Zhang, J. Beckett, M. Mascal, A. J. Moulé, *Macromolecules*, 2017, **50**, 5476.

45) I. E. Jacobs, E. W. Aasen, D. Nowak, J. Li, W. Morrison, J. D. Roehling, M. P. Augustine, A. J. Moulé, *Advanced Materials*, 2017, **29**, 1603221.

46) V. Untilova, J. Hynynen, A. I. Hofmann, D. Scheunemann, Y. Zhang, S. Barlow, M. Kemerink, S. R. Marder, L. Biniek, C. Müller, M. Brinkmann, *Macromolecules*, 2020, **53**, 6314.

47) A. Hamidi-Sakr, L. Biniek, J.-L. Bantignies, D. Maurin, L. Herrmann, N. Leclerc, P. Leveque, V. Vijayakumar, N. Zimmermann, M. Brinkmann, *Advanced Functional Materials*, 2017, **27**, 1700173.